Residual stresses of friction melt bonded aluminum/steel joints determined by neutron diffraction

N. Jimenez-Mena[1], T. Sapanathan[1, *], J.M. Drezet[2], T. Pirling[3], P. J. Jacques[1], A. Simar[1]

[1] Institute of Mechanics, Materials and Civil Engineering, UCLouvain, B-1348 Louvain-la-Neuve, Belgium

[2] École Polytechnique Fédérale de Lausanne, Institut des Matériaux, station 12, 1015 Lausanne, Switzerland

[3] Institut Laue-Langevin, 71 avenue des Martyrs, CS 20156, 38042 Grenoble cedex 9, France

* Corresponding author e-mail: thaneshan.sapanathan@uclouvain.be

Abstract

Near interfacial residual stresses are investigated in a joint composed of aluminum alloy and dual phase steel. A small step neutron diffraction scan was initially performed to determine the weld interface position along the measured transverse cross section. Residual stress measurements were then performed in three orthogonal directions for steel and aluminum using {211} and {311} diffraction peaks, respectively. The small step scan enables to identify the wavy nature of the interface, which has been subsequently combined in the residual stress calculation. The resultant of all three components of the residual stresses is almost zero along the mid-thickness of the steel plate, validating the estimated stresses. Near the interface, residual stresses on the steel reveal an "M" shape distribution while in the aluminum sheet they show a "W" shape. The interfacial residual stresses in the steel originate from the thermomechanical processing condition, phase transformation and the mismatch in the coefficients of thermal expansion (CTE). At the vicinity of the interface, the aluminum plate presents a distribution of residual stresses similar to a superposition of residual stresses resulting from an arc welding and the effect of mismatch in CTE.

Keywords: dissimilar welds, residual stresses, interface, neutron diffraction, aluminium, dual phase steel

Nomenclature

d_0^{hkl}	Inter planar distances (Å)
E^{hkl}	Young's modulus specific to the crystallographic orientation (GPa)
v^{hkl}	Poisson's ratio specific to the crystallographic orientation
Z_{IGV}	Centroid position of the instrument gauge volume
Z_{SGV}	Centroid position of the instrument gauge volume
α_{Al}	Coefficient of thermal expansion of Al (°C^{-1})
α_{steel}	Coefficient of thermal expansion of steel (°C^{-1})
2θ	Peak position (degree)

$\varepsilon_{xx}, \varepsilon_{yy}$ and ε_{zz}	Longitudinal, transverse and normal residual strain components, respectively
ε_{Al}^{th}	Thermal expansion in Al
ε_{steel}^{th}	Thermal expansion in steel
ε_{int}	True deformation at the interface
λ^{hkl} and μ^{hkl}	Lamé's elastic coefficients specific to the crystallographic planes (MPa)
σ_{xx}, σ_{yy} and σ_{zz}	Longitudinal, transverse and normal residual stress components, respectively (MPa)
σ_{SS} and σ_{SA}	Residual stresses on a given surface of steel and aluminum, respectively

1. Introduction

Welding of Al/steel brings challenges related to the metallurgical compatibilities of those two materials. Simar and Avettand-Fènoël (2017) reviewed various cases of dissimilar welds and reported that the large differences in melting temperatures and coefficients of thermal expansion (CTE) of both aluminum and steel and the formation of a brittle intermetallic (IM) layer at the interface reduce the mechanical integrity of the joints.

Solid state welding techniques, such as Friction Stir Welding (FSW) or inertia friction welding and liquid state methods such as laser welding or arc welding lead to the formation of intermetallic compounds at the interface. According to Tanaka *et al.* (2009), the thickness of the IM layer drastically influences the toughness of the joint. They demonstrated a significant improvement in the fracture toughness with the IM thicknesses below 1 µm. Although, the desired thickness of the IMs is often below 1 or 2 µm for aluminum-steel welds, the low advancing speed or high input power of many welding processes lead to the formation of thick IMs.

To overcome the existing challenges and achieve a good quality multi-metallic joint, van der Rest *et al.* (2013) recently patented a new process called "Friction Melt Bonding (FMB)". Jimenez-Mena *et al.* (2018) further investigated the process to join aluminum to steel with advancing speeds as fast as 1000 mm/min. The IM thickness can thus be significantly reduced. FMB is particularly suitable for a lap welding configuration where the upper steel plate is heated locally by friction stirring using a simple rotating cylindrical tool powered by a generic milling machine. van der Rest *et al.* (2014) also reported that the heat generated during the process locally melts the aluminum and forms one or more IM compounds (e.g. Fe_2Al_5 and $FeAl_3$). The FMB of Al/steel does not require any protective environment since the molten pool of Al is confined within the assembly without having a direct contact with the atmosphere.

According to Smith (1979), residual stresses at the welded joints particularly affect the mechanical properties, performance under fatigue loading, load bearing capacity of the structures and crack propagation. For instance, a study performed by Deplus *et al.* (2011) for an aluminum weld produced by FSW reveals large tensile residual stresses in the center of the processed zone and compressive residual stresses in the surrounding heat affected zone (HAZ). Residual stress distributions for welds between two different aluminum alloys investigated by Prime *et al.* (2006) and between two different steels by Joseph *et al.* (2005). However, few works were performed for the residual stress measurements on dissimilar metal welds (e.g.Al/steel). Recently, Agudo *et al.* (2008) performed residual stress measurements using synchrotron X-Ray diffraction for the dissimilar combination of AA5182 and DX54D steel in a butt-welded joint fabricated by a cold metal transfer (CMT) technique with an aluminum based filler material. Since CMT technique is a modified gas metal arc welding technique, the residual stresses observed with CMT were shown to agree with a typical arc welding without significant influence of the phase transformation. Moreover, a neutron diffraction study was conducted by Gan *et al.* (2017) to investigate the residual stresses in a rotatory friction welded AA7020/AISI-316L stainless steel joints. Their study reported the residual stresses in cylindrical coordinate system, for radial, hoop and axial components and identified that AA7020 and AISI-316L have tensile and compressive residual stresses, respectively. Another study carried out by Kim *et al.* (1995) on residual stresses for a titanium/AISI-304L stainless steel joint made by rotatory friction welding using numerical simulation. They predicted that, at the vicinity of the interface, the radial component of residual stresses is tensile in AISI-304L while titanium presents compressive residual stresses. This was explained by the larger CTE of steel compared to that of titanium. Besides, the axial component of residual stress at the interface near the periphery of the welded rods of AISI-304L and titanium is predicted as compressive and tensile, respectively. This result was attributed to the limited stiffness of titanium compared to steel.

Although their model considers the thermomechanical aspects of the process, metallurgical changes such as phase change or intermetallic formation have been ignored.

All those aforementioned examples are performed in a butt welding or a rotatory friction welding configuration whereas a lap welding configuration is used in the present study. In addition, the consequences of the presence of pseudo strain at the interface region (Section 3) and the various contributors to the residual stresses should be investigated. This is the primary focus of the present study. Neutron diffraction enables to carry out this investigation owing to the high penetration depth of neutrons in metals. According to Hutchings *et al.* (2005), this technique is also a suitable method for large sample thicknesses (e.g. 60 mm in steel and 300 mm in aluminum (Pirling, 2011)) and has the capability to measure 3D stress components. In the present work, a pseudo strain correction algorithm is also implemented to carefully post process the near interface measurements.

2. Experimental procedure

2.1. FMB process and coordinate system

A schematic view of the FMB process is shown in Fig. 1a. Welding by FMB is performed in a lap configuration with the steel plate on top of the aluminum plate. The rotating flat faced, 16 mm diameter, cylindrical tungsten carbide (WC) tool locally generates sufficient heat by friction, to locally melt the aluminum below the tool and subsequently creates the bond with the steel plate. The selected coordinate system with respect to the tool movement and the welding direction is provided in Fig. 1b, i.e. longitudinal direction along the welding direction, transverse direction perpendicular to the welding direction, and normal direction along the tool axis.

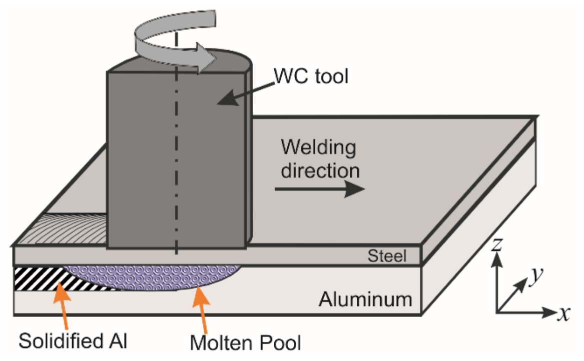

(a)

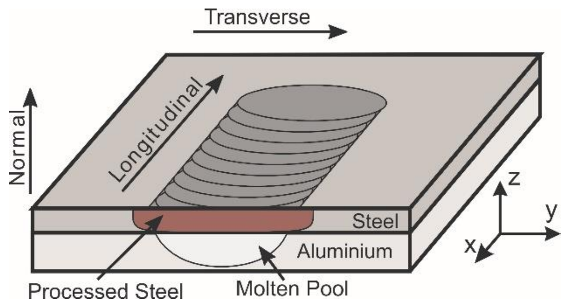

(b)

Fig. 1. (a) Schematic illustration of a longitudinal section view showing the FMB process in the case of an aluminum-steel assembly in a lap welding configuration. (b) Coordinate system (longitudinal, transverse and normal directions) used in this study.

2.2. Materials and welding conditions

The investigated welds were performed using a Hermle UWF 1001H universal milling machine. The welds were carried out with a tool advancing speed of 300 mm.min^{-1} and a rotational rate of 2000 rpm. The dimensions of the plates were 200 mm x 80 mm (L × W) with the weld length of ~165 mm.

The base materials were Dual Phase steel (DP600) sheet (0.9 mm thickness) and an aluminum alloy plates (3.1 mm thickness). The microstructure of the base DP600 steel is shown in Fig. 2a and b. It shows two constituent phases: the polygonal ferrite and martensite (Fig. 2a and b). In order to avoid texture owing to the directional solidification of the molten pool of the Al alloy (Fig. 2c) that could influence the intensity of the diffraction peaks, 2% of Al-5Ti-1B (grain refiner) was added to the AA1050 in a prior casting process to obtain an equiaxed microstructure (Fig. 2d). The casting was performed in a vacuum furnace followed by a cold rolling step to obtain a 3.1 mm thick Al plate. Then, plates were machined to 200 mm × 80 mm (L × W).

During casting of AA1050 with the grain refiner, the grains became equiaxed and were surrounded by a eutectic phase. The cold rolling process elongated the grains while the eutectic was redistributed along the rolling direction. To minimize the accumulation of residual stresses during the fabrication of the Al plates (casting and cold rolling), they were annealed at 350°C for 2 hours and furnace-cooled prior to FMB. During the annealing step, recrystallization was expected. However, it was noticed that the temperature was not sufficient to dissolve the iron-rich inclusions into the Al matrix and thus the recrystallized grains grow around them.

The chemical composition of DP600 steel and the grain refined Al alloy (AA1050+ 2% Al-5Ti-1B) obtained using inductively coupled plasma (ICP) mass spectrometry analysis are reported in Table 1. The mechanical behaviours of DP600 steel and Al are included in supplementary material.

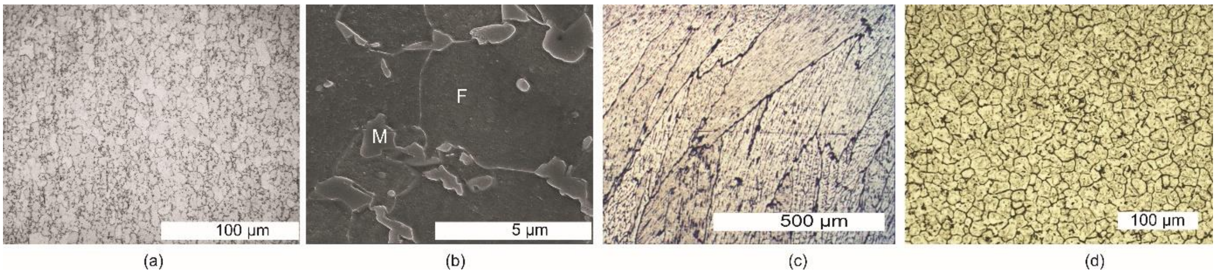

Fig. 2. Microstructures of base DP600 steel using (a) Light microscopy and (b) Scanning electron microscopy (SEM) at higher magnification [F – polygonal ferrite and M – martensite]. Light micrographs of (c) the solidified molten pool of as received AA1050; (d) the Al alloy material obtained after casting with the addition of 2% Al-5Ti-1B showing small equiaxed grains.

Table 1: Chemical composition of DP600 steel and the Al alloy (wt. %)

Alloying elements	Fe	Al	B	Mn	Si	Ti	Cr	Ni	C^{Total}
DP600 steel	97.40	0.03		1.93	0.24		0.20	0.02	0.04
Al alloy	0.36	98.60	0.02	0.01	0.06	0.12			

2.3 Neutron diffraction experiments

The neutron diffraction measurements were performed at Institue Laue-Langevin (ILL) with SALSA (Strain Analyser for Large and Small scale engineering Applications) instrument. Fig. 3a shows a welded sample mounted on the hexapod. More details of the hexapod degrees of freedom and the configuration of SALSA detectors are available in the early work of Pirling *et al*. (2006). A wavelength of 0.166 nm was used in these experiments. Diffraction planes of {211} for steel suggested by Jacques *et al*. (2006) and {311} for Al sugested by Chobaut *et al*. (2015), were considered for the measurments for DP600 and aluminum alloy, respectively. As shown in Fig. 3b and c, one can clearly distinguish between the steel and Al peaks since they do not overlap as they have different diffraction angles for the measured planes (i.e. {211} and {311} for steel and Al, respectively) even if the gauge volume probes both materials at the same time.

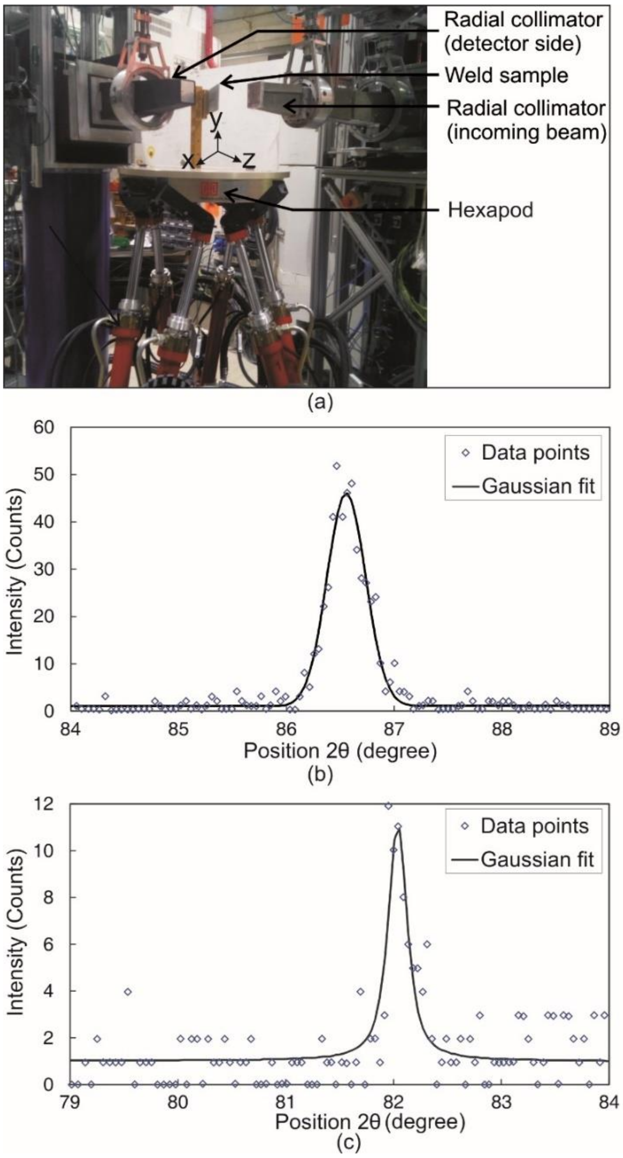

Fig. 3. (a) Welded specimen in longitudinal direction mounted on the hexapod of SALSA instrument while performing the neutron diffraction measurements. (b) Example of data fitting performed during the post processing for the case of steel showing {211} peak position for a 2θ range between 84° and 89°. (c) Example of data fitting performed for a diffraction of aluminum alloy {311} peak for a 2θ range between 79° and 84°.

The smallest nominal gauge volume (NGV) defined with SALSA, 0.6 mm × 0.6mm in the *xy* plane and the depth of 2.0 mm in *z* direction, was used in this experiment to obtain high resolution data across the Al/steel interface. However, according to ISO/TS 21432:2005 (2010) standard the instrument gauge volume (IGV) should consider the divergence of the beam. The geometry of the IGV was identified as 1.3 mm x 1.3 mm in the *xy* plane and the depth of 2.0 mm in *z* direction based on the fitting model of Bruno *et al*. (2006), and using the diffraction data obtained for the stress free ferritic steel plates which have the thicknesses of 0.23 and 0.31 mm. These stress free plates are used to obtain the fitting parameter for the pseudo stress correction. The identified IGV and the fitting parameters were used in the subsequent calculations. Pirling

(2011) defines the IGV by the beam shaping optics, while the actual sampled gauge volume (SGV) is given by the interaction between the IGV and the sample. The SGV can vary with the relative probing position. That is, SGV is smaller in the cases of partial immersion of the IGV inside the sample. It should be noted that using the small NGV presents the disadvantage of increasing the acquisition time. Each scan was thus performed with 500 counts which was large enough to provide adequate statistics of the diffraction peak while taking a maximum of 15 minutes for low diffracting points in aluminum.

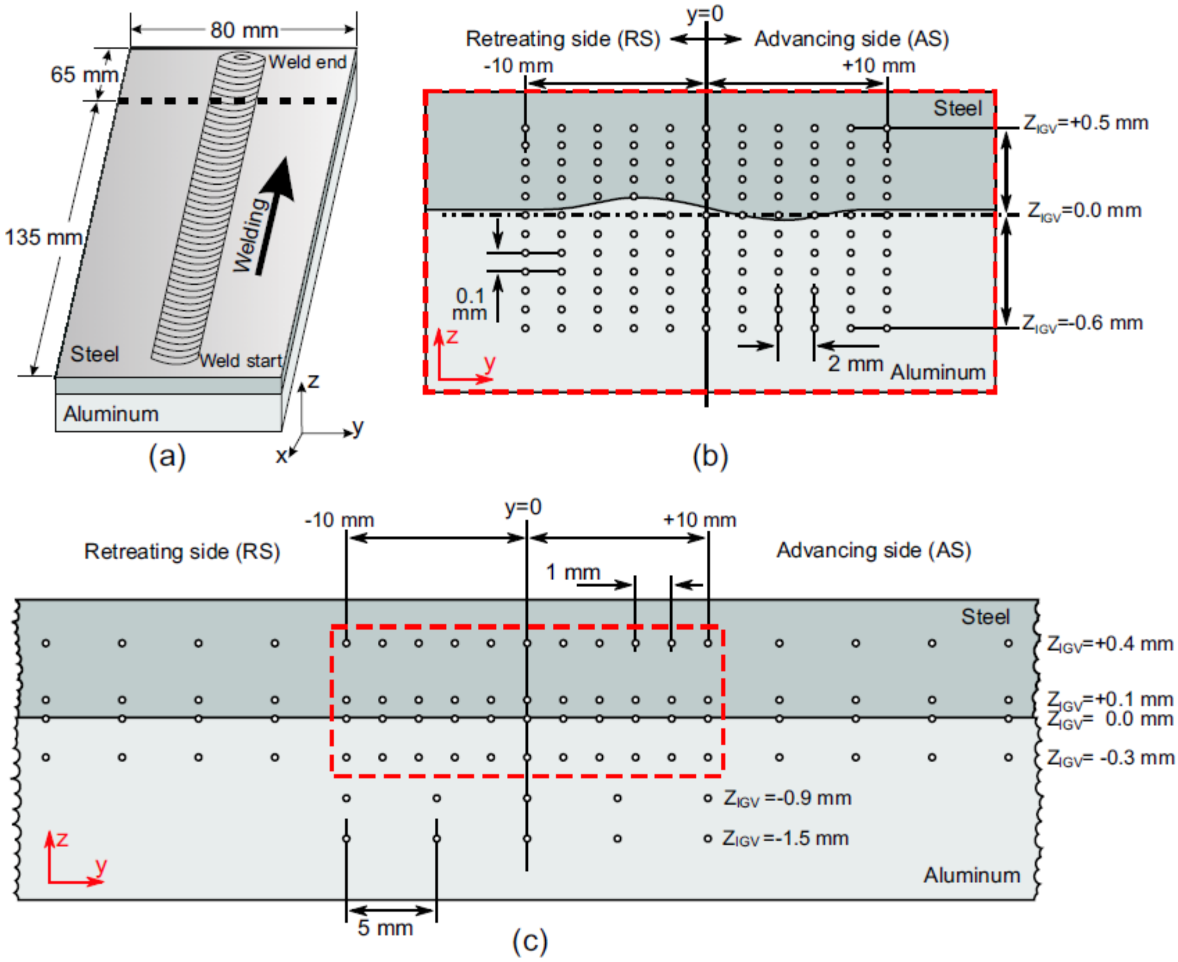

Fig. 4. (a) Schematic illustration of the location of the neutron diffraction scan indicated by the dashed line. Schematic representation of the analysed centroids of IGV (Z_{IGV}) for diffraction points for (b) the steel plate close to the interface used to track the interface and (c) line scans parallel to the interface in both steel and aluminum plates. The red dashed box in c indicate the location of the small step scan.

The diffraction scans were performed across the weld indicated by the broken line in Fig. 4a (at the steady state region and 135 mm in *x* direction from the starting side of the weld). Two distinct approaches were taken to scan both material and their interface. Firstly, the surroundings of the welded interface were probed for the steel to track the position of the interface (Fig. 4b). This was performed in a fine grid array including the processed zone defined by -10 mm ≤ y ≤ 10 mm (Fig. 4b). The second series of measurements were performed along the lines parallel to the interface for both aluminum and steel to obtain the profile of residual stresses on the transverse cross section of the entire plate (Fig. 4c). During this scan, the lines corresponding to positive Z_{IGV} were used to probe the residual stress measurements in the steel plate while the lines with $Z_{IGV} \leq 0$ probed the aluminum plate. The longitudinal and transverse components were measured in the transmission mode while the normal component was obtained using the reflection configuration.

Specimens from the base materials with the same plate thickness and having the dimensions of 3 mm × 3 mm (L × W) were used to obtain the reference inter planar distances (d_0^{hkl}). The identified reference inter planar distances (d_0^{hkl}) for DP600 steel along {211} and the aluminum alloy along {311} planes were 1.167 ± 0.001 Å and 1.217 ± 0.001 Å (corresponding to the 2θ values of 86.514° and 82.160°), respectively. These results were later used in the residual stress calculations. Moreover, d0 values of the parent materials were obtained at various location in through thickness indicating nearly the same, thus it confirms that the anisotropy due to rolling in the sample is negligible. It was also expected that the rolling history will not remain in the plates due to the annealing treatment prior to welding and the thermal cycles experienced by the sample during the process. Moreover, the flow characterization of the material (Fig. S1 in supplementary material) shows that the parent materials present a negligible anisotropy; we thus expect that the d0 value is not orientation dependent for both steel and aluminum.

The aluminum plate was made by casting, rolling and then annealing before welding and has high purity (98.6%). Therefore, we use the parent d0 for the case of aluminum as a reliable measurement. Moreover, at the vicinity of the interface (at $Z_{IGV} = 0$) the measurements for aluminum may be highly influenced by the intermetallic formation, so that could be a reason for significant fluctuations of the corresponding strain measurements at $Z_{IGV} = 0$. So, the corresponding line scan measurements were completely avoided in the analysis. The thermal cycles during FMB are also very short, so the resulting dissolution phenomena of Al into Fe and Fe into Al are confined to few microns around the interface. Thus, the solubility of iron in Al and vice-versa is negligible and the lattice constants are expected to be barely affected by the solid solution phenomenon in the various residual stress measurement locations.

In the case of steel, peak splitting effect between ferrite and martensite was not observed, thus a resulting mean peak was considered for the peak fitting and stress free reference sample in this study. This effect could be resulting from the low carbon content (0.04%) in the steel. Therefore, the reliable constant d0 values obtained from the parent steel is also used to estimate the residual stresses.

Neutron diffraction data was processed using the LAMP (2017) software to obtain the peak position (2θ) and other relevant information such as maximum normalized intensity and Full Width at Half Maximum (FWHM). It should be noted that the normalized intensity is defined by the area of the fitted peak divided by the acquisition time. Following the computation of individual strain components using Bragg's law, residual stresses (σ_{xx}, σ_{yy} and σ_{zz}) were calculated using the generalized Hooke's law (Eq. 1-3) for three orthogonal directions:

$$\sigma_{xx} = 2\mu^{hkl}\varepsilon_{xx} + \lambda^{hkl}\,(\varepsilon_{xx} + \varepsilon_{yy} + \varepsilon_{zz}) \tag{1}$$

$$\sigma_{yy} = 2\mu^{hkl}\varepsilon_{yy} + \lambda^{hkl}\,(\varepsilon_{xx} + \varepsilon_{yy} + \varepsilon_{zz}) \tag{2}$$

$$\sigma_{zz} = 2\mu^{hkl}\varepsilon_{zz} + \lambda^{hkl}\,(\varepsilon_{xx} + \varepsilon_{yy} + \varepsilon_{zz}) \tag{3}$$

where, λ^{hkl} and μ^{hkl} are Lamé's constants defined for the studied family of crystallographic planes as in Eq. 4 and 5;

$$\lambda^{hkl} = \frac{v^{hkl}E^{hkl}}{(1 + v^{hkl})(1 - 2v^{hkl})} \tag{5}$$

$$\mu^{hkl} = \frac{E^{hkl}}{2(1 + v^{hkl})} \tag{6}$$

and $\varepsilon_{xx}, \varepsilon_{yy}$ and ε_{zz} are longitudinal, transverse and normal strain components, respectively. v^{hkl} and E^{hkl} are the crystallographic Poisson's ratio and Young's modulus for the observed family of planes (Table 2), respectively.

Table 2 : Material parameters for the selected crystallographic orientations given by Hutchings *et al.* (2005)

Materials	Investigated crystallographic plane	v^{hkl} (dimensionless)	E^{hkl} (GPa)
DP600 steel	{211}	0.28	225.5
Al alloy	{311}	0.35	70.2

The calculated residual stresses were further treated with pseudo-strain correction to eliminate artificial peak shift due to the partial immersion of the gauge volume in another material at the vicinity of the interface. Further details of the pseudo-strain correction principles are given in Section 3. The statistical errors were calculated for the peak position based on the fitting algorithm according to the method proposed by Chobaut (2015). The obtained raw data of this experiment by Jimenez-Mena *et al.* (2017) are made available in the ILL data depository.

3. Pseudo strain origin and correction

Wang *et al.* (1998) reported that the neutron diffraction for near surface measurements are challenging due to partial immersion of the gauge volume in the sample that can cause anomalous peak shifts. Thus, according to Ezeilo *et al.* (1991), X-ray diffraction was used to measure the residual stresses near the surface while in depth measurements were performed using neutron diffraction technique. However, for an interface or an internal free surface which does not have direct access, requires a depth of penetration, X-Ray measurements are not suitable.

The peak shifts anomaly at near-surface (free surface and interface) measurements, brings a pseudo-strain that deviates the center of the peak from its actual position and provides an erroneous value of strain measurements. Šaroun *et al.* (2013) reported various sources of pseudo-strain resulting from signal attenuation, peak clipping effect, inhomogeneous wavelength distribution and a geometrical origin due to the partial immersion of the sample in the IGV. However, most of these effects, except the geometrical origin, are suppressed by using a small gauge volume and a radial collimator. The remaining pseudo-strain resulting from the geometrical origin (i.e. the geometrical peak shift) still needs to be corrected.

Bruno *et al*. (2006) developed a geometrical model to calculate the position of the centroid of the SGV (Z_{SGV}) in partial burying conditions. Their geometrical model has been adapted in this work for the pseudo strain correction of interface measurements (see supplementary material for more detail). However, the exact position of the IGV with respect to the interface is not known at the beginning of the present study. Hence, the normalized intensity of the diffracted beam, obtained from the small step scan in the vicinity of the interface, is used to overcome this issue and to identify the interface position.

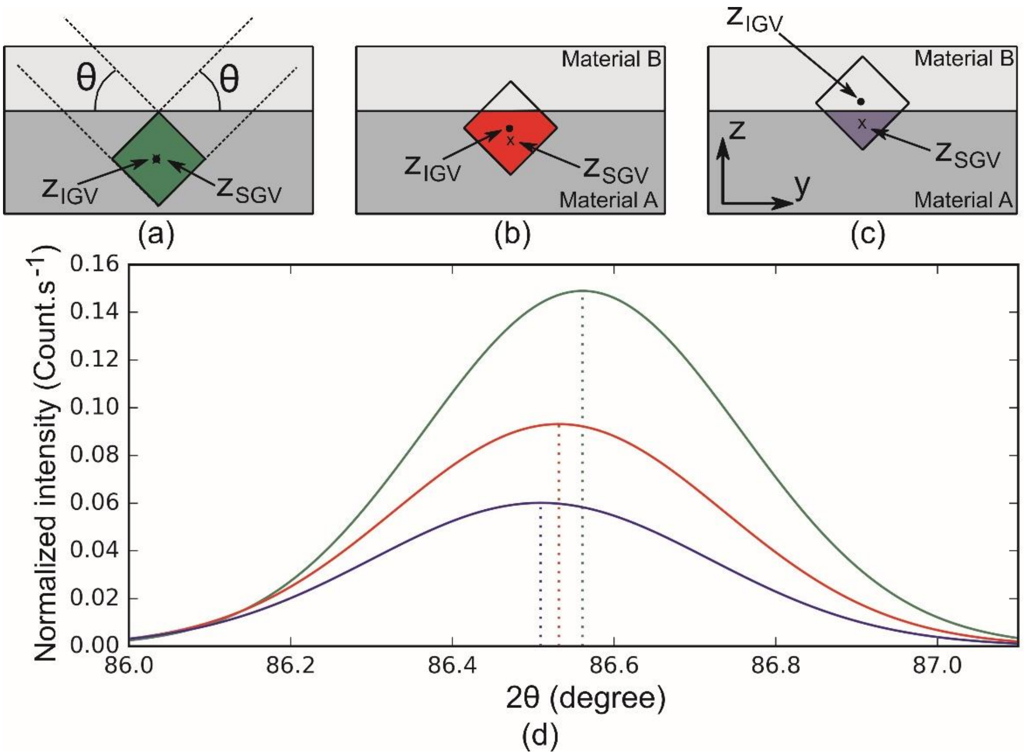

Fig. 5. Schematic representation of the sampled gauge volume (SGV, shaded by green, red and blue in a-c) with respect to the reference sample surface and its effect on the normalized intensity. The IGV is illustrated using a perfect rhombus shape in a-c. (a) Centroids of both IGV (Z_{IGV}) and SGV (Z_{SGV}) are coincident, when the gauge is fully immerged into the sample (Material A). Material B could either be air at free surface or another material at an interface. The centroids move apart when the gauge volume is partially inside the sample (b and c). (d) Normalized intensity variation and peak position for the corresponding SGV presented in schematic of a-c. [θ – incidence angle of the beam]

Schematic illustrations in Fig. 5a-c, showing the evolution of the normalized intensity with the peak position as the IGV traverses the interface from material A to material B, illustrate an example of the geometrical peak shift for a reflection configuration. The partial immersion of IGV also results in the decrease of peak normalized intensity (Fig. 5d). The change in normalized intensity thus enables to determine the interface position. The identified interface position is incorporated within the geometrical model of Bruno *et al*. (2006), and used in the artificial shift correction of the near interface residual stresses.

4. Results and discussion

4.1 Interface tracking with neutron diffraction

From previous experimental observations, it was identified that FMB interface exhibits a wavy shape as the result of the plastic flow of steel from the retreating side (RS; i.e. $y < 0$) to the advancing side (AS; i.e. $y > 0$). From the initial scans on the reference samples of the base materials, diffraction intensities are identified as ~1.7×10^{-1} and ~1.6×10^{-2} (count.s^{-1}) for steel and aluminum, respectively, when the IGV is at the center of the samples. It indicates that the normalized intensity in steel is one order of magnitude higher than that in aluminum. Therefore, the change in normalized intensity of steel is used to track the position of interface based on the small step diffraction measurements (Fig. 4b). The normalized intensity decreases as Z_{IGV} leaves the steel plate perpendicularly towards the Al plate. To accurately predict the value of Z_{SGV}, the evolution of the normalized intensity of the steel {211} peak for a fixed y with varying Z_{IGV} positions is compared to the intensity profile predicted by the model. Once the best fitting has been obtained, the corresponding shift has been recorded as the interface position. Fig. 6a and b show the evolution of the normalized intensity in the normal direction of the steel peak ({211} peak) versus the position of Z_{IGV}, for the scans along the z direction, at y=-4 mm and y=+4 mm, respectively. Similarly, this procedure has been repeated for each y values, for both normal and transverse measurements obtained from the small step scan. Hence, diffraction measurements of both the normal and transverse directions are used to predict the interface position. The measurements in the longitudinal direction are not used due to the lower lateral resolution resulting from the orientation of the IGV with respect to the sample.

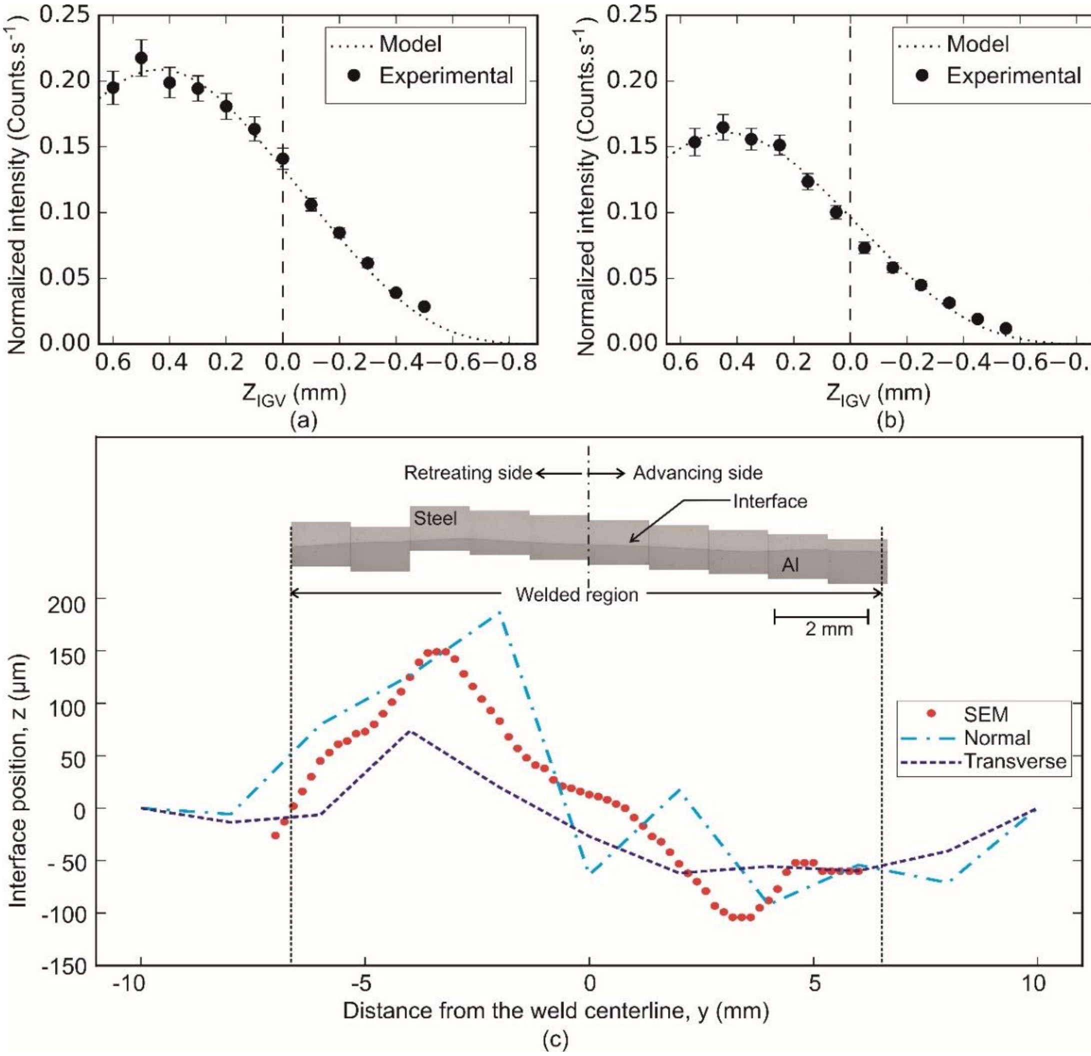

Fig. 6. Evolution of the normalized intensity obtained from the interface scan for the normal direction along z and fitted with the corresponding mathematical model at (a) y = -4 and (b) y = +4 to identify the interface positions. The Z_{IGV} is at the interface when the relative normalized intensity of the steel peak (i.e. {211} peak) decreases approximately 50% of the maximum normalized intensity. (c) Comparison of the interface tracking using the diffraction intensities in the normal and transverse direction with the measurements performed on the transverse cross-section using SEM after dissecting the sample from the corresponding interface. Light microscopy image of the Al/steel FMB weld revealing the wavy shape of the interface is enclosed in (c).

After the neutron diffraction experiments, the welded sample was dissected at the location where the neutron measurements were performed (Fig. 4a). Optical micrograph of this transverse cross-section shown in Fig. 6c reveals the wavy shape of the Al/steel interface where the steel plate shows a slight penetration into the aluminum plate on the AS while the opposite is noticeable on the RS. Fig. 6c shows a comparison between the estimated results based on the neutron diffraction and the shape of the interface extracted from the SEM observations on the transverse cross-section.

The neutron diffraction measurements in the normal and transverse directions predict the peak-to-peak values for the wavy interface of approximately 275 and 125 μm, respectively (Fig. 6c). These values reasonably agree with the measurement carried out in SEM of about 250 µm. Thus, the neutron diffraction measurements provide an interesting nondestructive method to track the interface position. The deviation from SEM measurements might be in part, due to the averaging of the signal in the interaction volume and any misalignment of the sample with respect to the reference axis set during the measurements. The Al-steel interface measured using the normalized diffraction intensity in normal direction is then incorporated in the pseudo correction algorithm. The interface position based on the normal intensities is more accurate due to the highest diffraction intensity obtained in the normal direction (see Section 4.2).

4.2 Microstructure effect on diffraction peaks

The heterogeneous microstructure also affects the maximum intensities of the diffracted beam. The maximum intensities obtained for the three orthogonal directions (longitudinal, transverse or normal) for various zones of both steel and aluminum are given in Table 3. The maximum normalized intensity also depends on the orientation. Particularly for steel, the normalized intensity in longitudinal and transverse directions are ~50% of that in the normal direction. This could be explained by the presence of a crystallographic texture in the base metal. Nevertheless, due to the low diffraction intensities of the aluminum alloy, the change in normalized intensity cannot clearly be detected (Table 3). Table 3 clearly indicates that the normalized intensity in aluminum is one order of magnitude lower compared to steel.

Table 3: Maximum normalized intensities in the steel and Al, in counts.s^{-1}, listed with diffraction orientations.

	Longitudinal	Transverse	Normal
Base Steel	0.13	0.17	0.30
Processed Steel	0.14	0.15	0.20
Base Aluminum	0.010	0.012	0.010
Aluminum molten pool	0.015	0.015	0.011

The drop of the maximum normalized intensity in the processed zone of the steel can be related to the as-quenched state of the martensite. Watherschoot *et al.* (2003) observed that the normalized intensity of the {211} planes in the as-quenched state was lower than that obtained after a heat treatment. Fig. 7a shows that the FWHM of the diffraction peaks in the different directions clearly increase in the processed zone compared to the base material. As shown in Fig. 7b-e this increase results from the modification of microstructure with a wider peak (i.e. larger FWHM) corresponding to almost fully martensite (Fig. 7d) and a narrow peak corresponds to the dual-phase microstructure (Fig. 7e). Neutron diffraction measurements thus have the additional capability to accurately track the position of the processed zone and highlight a change of microstructure in a nondestructive manner.

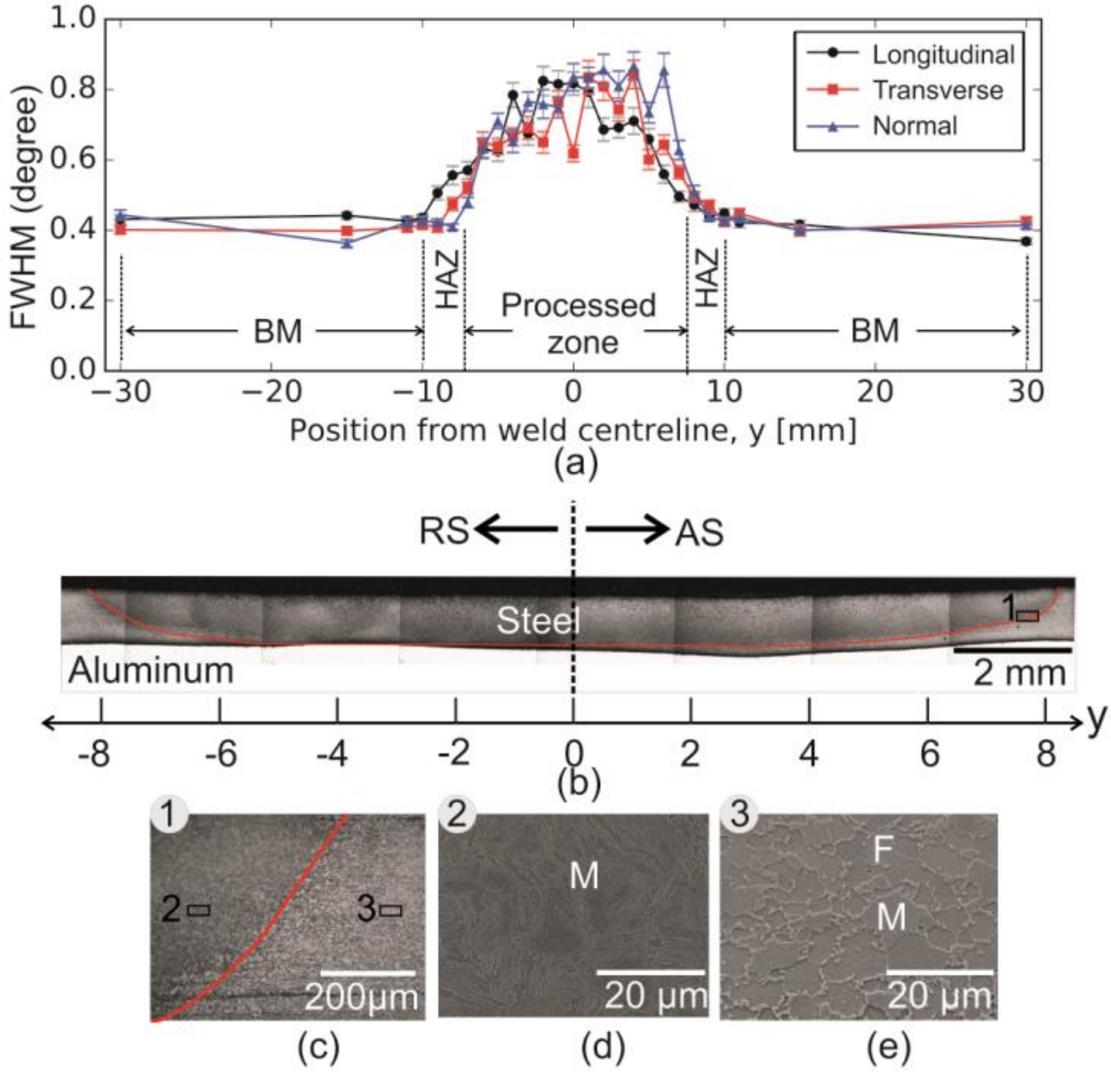

Fig. 7. (a) Full width at half maximum (FWHM) of the {211} diffraction peak, in all three orthogonal directions on the transverse position obtained from the Gaussian data fitting, correspond to the line scan measurements along the Z_{IGV} = 0.4. (b) Light microscopy observation of the etched steel used for a comparison between the parent and processed zones with the FWHM. Microstructure at the regions along the interface between the fully martensite and a transition zones in [c and box 1 in b], martensite structure [d and box 2 in c] and dual-phase microstructure [e and box 3 in c]. (BM – base material, M – martensite and F - polygonal ferrite)

4.3 Residual stresses

Horizontal line scans (Fig. 4c) are used with a constant SGV to investigate the residual stress profiles in both DP steel and aluminum alloy. Residual stresses obtained for the line scan in the steel at Z_{IGV} = 0.4 mm are shown in Fig. 8a-c. For the steel plate, maximum longitudinal residual stresses are tensile in the longitudinal direction near y = ± 10 mm from the weld centerline (Fig. 8a and d). Along the mid-thickness (Z_{IGV} = 0.4 mm), steel accommodates the maximum longitudinal tensile residual stress of 282 ± 38 MPa that appears on the AS. For the same line scan along the Z_{IGV} = 0.4 mm, RS shows a maximum longitudinal tensile residual stress of 250 ± 44 MPa. The maximum compressive longitudinal stress obtained on the AS and RS along the mid-thickness of steel are -164 ± 31 MPa and -136 ± 27 MPa, respectively.

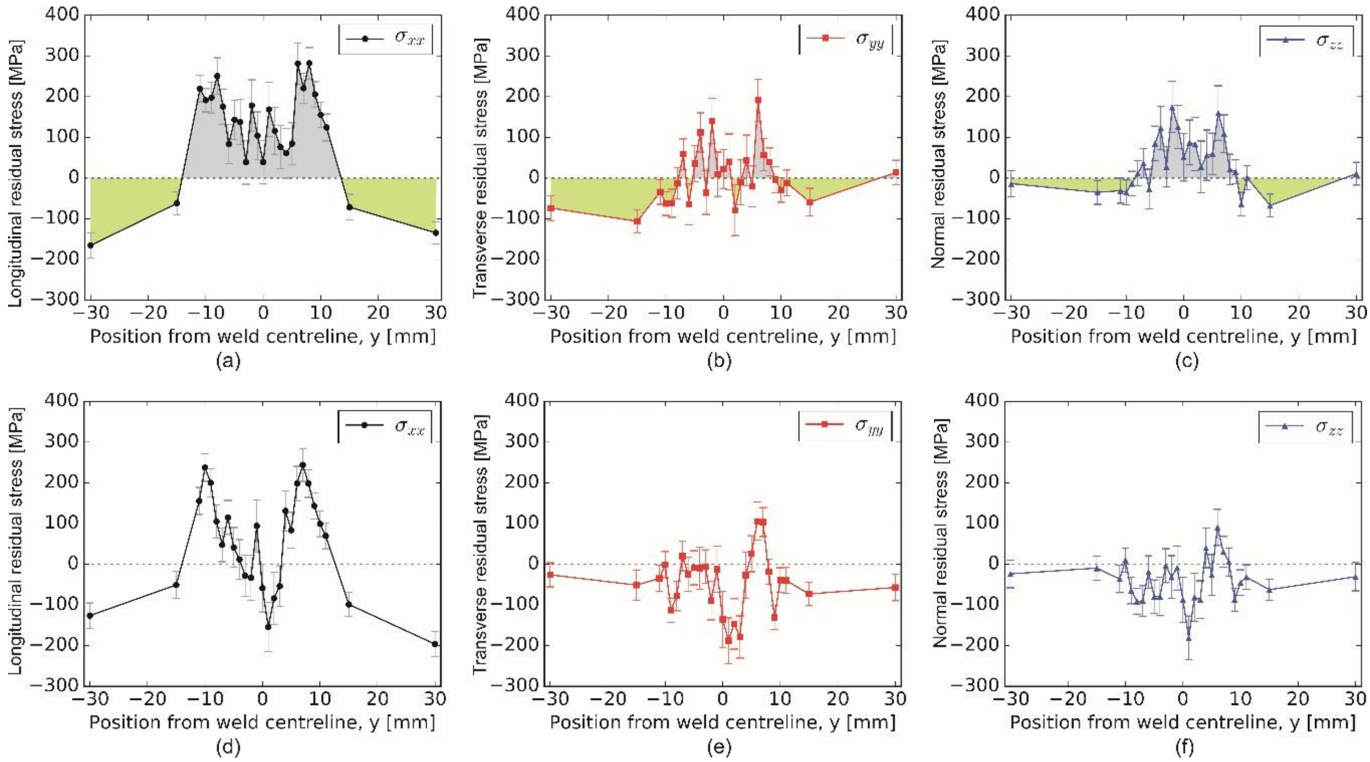

Fig. 8. (a) Longitudinal, (b) transverse and (c) normal components of residual stresses obtained for the welded plate along the mid-thickness of the steel corresponding to the line scan performed at Z_{IGV} = +0.4 mm. Near interface residual stresses on the steel side obtained for the (d) longitudinal, (e) transverse and (f) normal directions from the line scan along the Z_{IGV}= +0.1 mm. Residual stresses at Z_{IGV}= +0.4 is shaded by grey and green for tensile and compressive stresses, respectively in a-c. Error bars were calculated for the fitting peak position according to the method proposed by Chobaut (2015).

When Z_{IGV} = 0.4 mm, the SGV covers almost the entire thickness of the steel plate. Therefore, the estimated stresses corresponding to the particular line scan (Fig. 8a) can be considered as an average in the steel plate along its mid-thickness. In the particular measured plane, balance of forces is given by Eq. 7:

$$\int_{SS} \sigma_{SS} d_{SS} + \int_{SA} \sigma_{SA} d_{SA} = 0 \tag{7}$$

The first and second terms in the equation correspond to the forces on the steel and aluminum, respectively. SS and SA refer to the surface on the steel and surface of the aluminum, respectively. Considering the balance of forces on the steel plate itself, the contribution coming from aluminum is almost negligible due to the low yield strength of the aluminum alloy used in these experiments. Therefore, the average stresses in the steel is expected to be balanced by itself. It is in good agreement with the longitudinal residual stresses (Fig 8a). Clearly, these stresses show a balance of both tensile (highlighted in grey) and compressive (highlighted in green) components along the mid-thickness of the steel. Moreover, the same behavior is noticeable for the transverse and normal components of the residual stresses (Fig. 8b and c).

Residual stresses obtained for the line scan corresponding to near interface on the steel side (Z_{IGV} = 0.1 mm) are shown in Fig. 8d-f. Particularly the longitudinal residual stresses along the near interface scan clearly indicate an "M" shape distribution while it has the maximum tensile residual stress of 243 ± 40 MPa. The longitudinal residual stresses near the center of the weld at the interface become compressive and it has the maximum value of -153 ± 60 MPa.

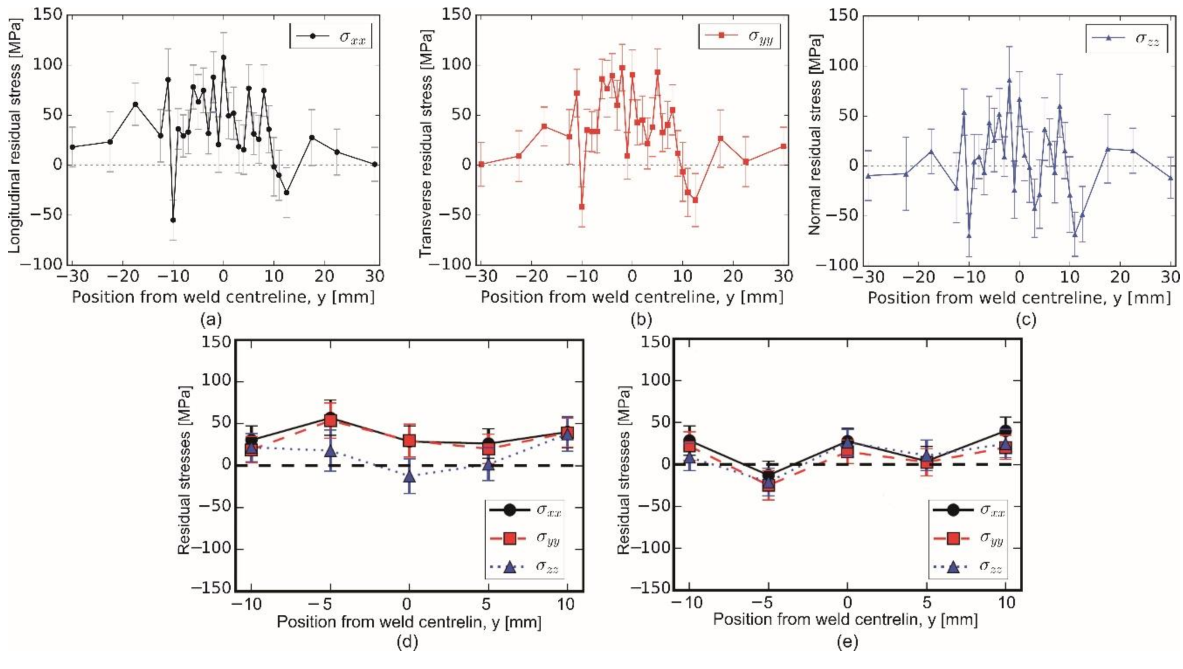

Fig. 9. Near interface residual stresses on the aluminum side obtained for the (a) longitudinal, (b) transverse and (c) normal directions from the line scan along the Z_{IGV}= -0.3 mm. Other residual stress components in the aluminum correspond to the lines at (d) Z_{IGV} = -0.9 mm and (e) Z_{IGV} = -1.5 mm. Error bars were calculated for the fitting peak position according to the method proposed by Chobaut (2015).

The lines scans corresponding to the Z_{IGV} = 0, -0.3, -0.9, -1.5 mm were used to measure the residual stresses in the aluminum plate (Fig. 4c). The measurements obtained for Z_{IGV} = 0 are omitted as they provide significantly low diffraction intensity due to the combined effect of near interface location (corresponding to small SGV) and low diffraction of the Al alloy (Table 3). The line scan corresponding to Z_{IGV} = 0 may also influenced by the formation of intermetallic owing to a maximum thickness of 10 µm in this particular welding case. Other line scan results obtained from the aluminum region are provided in Fig. 9a-e.

The residual stresses in the Al alloy show large fluctuations compared to the steel due to the weak diffraction intensity from Al. However, the results in Fig. 9a-c indicate that the different components of residual stresses are slightly tensile near the interface at the center of the weld. When moving away from the centerline, the residual stresses become slightly compressive near the locations where steel presents the highest longitudinal tensile residual stresses (i.e. near y = ± 10 mm). Moreover, the measurements obtained far from the interface for the Al alloy show a maximum of 50 MPa in tension for both the longitudinal and transverse components, while the normal stress is almost zero (Fig. 9d).

4.4 Origins of interface residual stresses

Measurements of residual stress obtained for Z_{IGV}= 0.1 mm and -0.3 mm respectively in steel and aluminum bring the explanation of the major origin for the residual stresses in the vicinity of the interface. Particularly, the trend in aluminum and steel in the longitudinal direction exhibits a mirroring effect in the vicinity of the interface (Fig. 8d and 9a). It is clearly evidenced that steel presents an overall "M" shape distribution while aluminum shows a "W" shape of residual stress distribution at the interface. Near the interface, while the steel presents the largest longitudinal tensile residual stresses, aluminum shows compressive longitudinal residual stress at those corresponding locations (Fig. 8d and 9a). The origins of this behavior in residual stresses are identified and explained in Sections 4.4.1 and 4.4.2 for steel and aluminum, respectively.

4.4.1 Residual stresses in steel plate

The profile of residual stresses in the steel plate may be explained based on the similarity of the FMB process on the steel side with the FSW of steel, apart from the absence of a tool pin. Kumar *et al*. (2013) identified that residual stress profile in FSW is caused by the non-uniform plastic deformation resulting from the inhomogeneous heating and cooling cycles and the allotropic phase transformation of steel during the process (Fig. 10a). Kou (2003) explained that the heat generated by friction causes the weld centerline to expand while surrounded by low temperature zones constraining their expansion. Plastic yielding occurs in the processed zone, so that the residual stresses remain after cooling down to ambient temperature. This sequence of expansion and contraction leads to tensile residual stresses ($\sigma_{xx} > 0$) in the processed zone and compressive stresses ($\sigma_{xx} < 0$) in the surroundings (Fig. 10a).

Crucifix *et al*. (2015) and Jimenez-Mena *et al*. (2018) investigated the temperature profiles of the FMB using both experimental and numerical methods. It was identified that the top surface of the steel reaches a temperature above 900°C (Fig 3 in Crucifix et al., 2015) and the aluminum that lies under the steel plate reaches a temperature larger than its melting temperature. Moreover, the complete martensite phase transformation at the top surface of the steel plate confirms that this steel must have reached a temperature larger than 890°C (AC3 temperature for this particular DP steel with a carbon content of 0.04%, Massalski et al. (1990)). The phase transformations occurring during cooling also contribute to the residual stresses in the steel plate. According to the Fe-C phase diagram, face centered cubic (FCC) austenite transform into less dense body centered cubic (BCC) ferrite (or bainite) or body centered tetragonal (BCT) martensite during cooling. Hence, the processed zone tends to expand during the cooling stage due to the transformation of the austenite and this expansion is constrained by the surroundings that did not transform to austenite. Compressive stresses thus appear, with a maximum at the weld centerline (Fig. 10a). The combined thermal effect and phase transformation result in the profile shown in Fig. 10a, where the maximum residual stresses are tensile and located on either side of the processed zone.

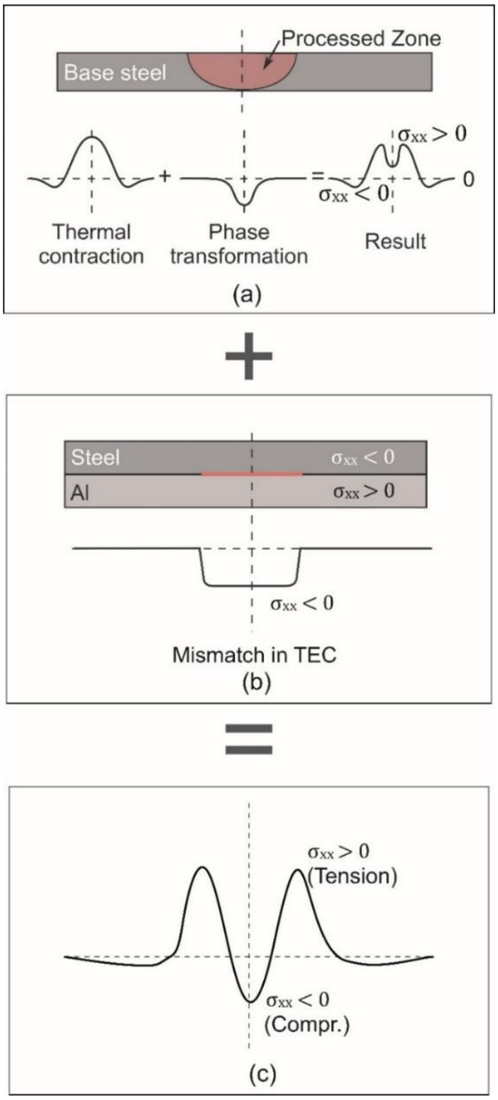

Fig. 10. Schematic illustration showing the origins of residual stresses for the steel plate close to the interface in an FMB joint in longitudinal direction; (a) residual stresses in the steel plate similar to the origins of FSW-process reported by Kumar *et al.*, 2013, (b) residual stresses due to bonding and subsequent cooling of materials with different CTE in a lap joint configuration and (c) superposition of the resultant {(a)+(b)} interfacial residual stresses in the steel plate.

Furthermore, residual stresses are also result from cooling of bonded plates with different CTE (Fig. 10b). Aluminum and steel have CTE of 23 and 14 µstrain/°C, respectively. When they are bonded together at high temperature and then cooled down to ambient temperature, the thermal contraction of the aluminum is approximately twice that of steel. The thermal expansion of Al and steel are given by $\varepsilon_{Al}^{th} = \alpha_{Al}\Delta T$ and $\varepsilon_{steel}^{th} = \alpha_{steel}\Delta T$, respectively. However, since they are bonded together, a constraint of identical deformation in the longitudinal and transverse directions is applicable at the interface. Therefore, the true deformation at the interface, ε_{int}, has a value in between that of the Al and steel plates, compared to what would have happened if they had contracted freely, i.e. $\varepsilon_{Al}^{th} > \varepsilon_{int} > \varepsilon_{steel}^{th}$. The steel plate thus contracts more than in the case of a free boundary resulting in compressive residual stresses after cooling (Fig. 10b), while the Al plate is subjected to tensile residual stresses (Fig. 11b), as will be explained in Section 4.4.2. The combined effect shown in Fig. 10a and b is schematically represented in Fig. 10c and is in good agreement with the longitudinal residual stress profile obtained for the steel plate (Fig. 8a and d). Moreover, the interfacial effect due to the mismatch in CTE becomes dominant close to the interface which can be clearly seen by comparing Fig. 8a and d. Indeed, near the interface (Z_{IGV}= +0.1mm), longitudinal residual stresses are highly compressive close to the centerline of the weld (Fig. 8d), while this is not as obvious for the line scans performed near the mid-thickness away from the interface (Z_{IGV} = +0.4mm, Fig. 8a).

4.4.2 Residual stresses in Al plate

Kou (2003) found the main origin of longitudinal residual stresses in the aluminum is resulted from the deformation caused by non-uniform thermal field and phase transformation similar to that occurring in an arc welding process. During the solidification of the molten pool and the subsequent cooling, the pool tends to shrink. However, the shrinkage is constrained by the surroundings that remained at lower temperature. Tensile residual stresses thus appear in the molten pool while the surrounding regions experience compressive residual stresses (Fig. 11a).

Furthermore, additional tensile residual stresses resulting from the mismatch of CTE (Fig. 11b), also accumulate with the arc welding like origin of residual stresses (Fig. 11a), since they both are positive (i.e, tension). Therefore, the resultant residual stress becomes tensile near the weld centerline while the surrounding regions have compressive residual stresses near the interface in the Al plate (Fig. 11c). This result also concurs with the experimental observations of the measured residual stresses in the Al plate (Fig. 9a).

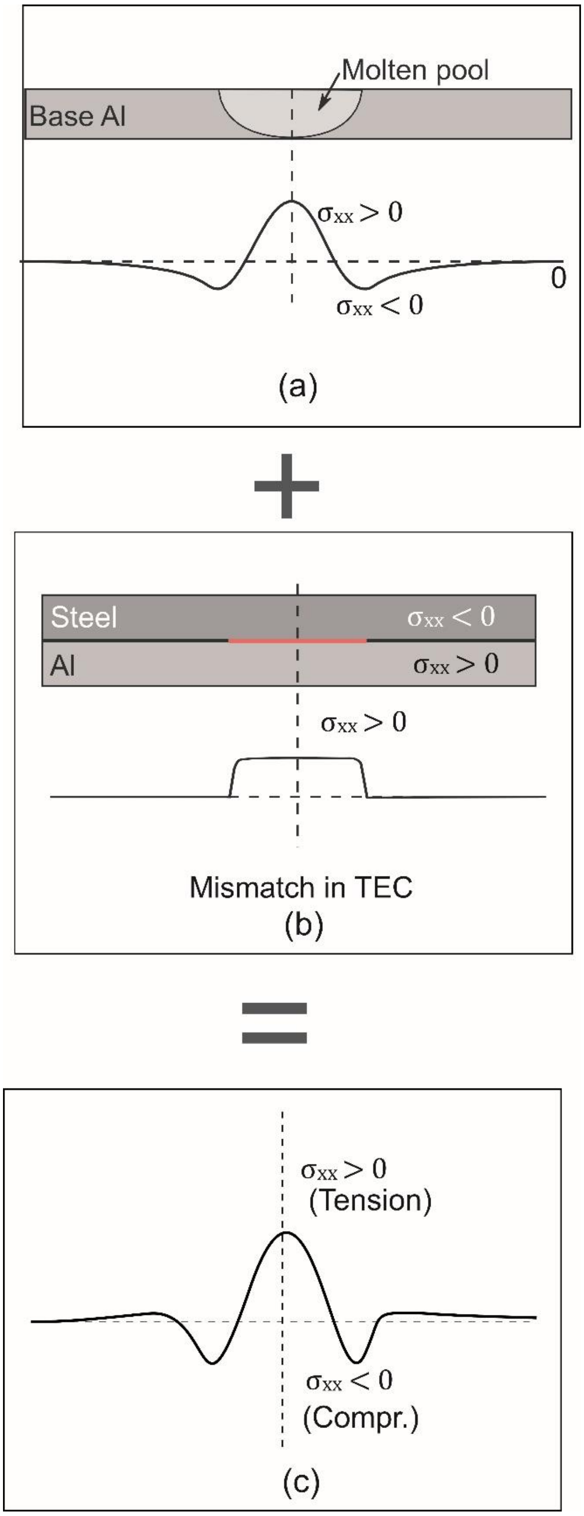

Fig. 11. Schematic profile of the longitudinal stresses in the welded Al at the interface resulting from two distinct phenomena; (a) residual stresses in the Al molten pool resulting from the origin similar to an arc welding process reported by Kou (2003), (b) residual stresses due to the bonding and subsequent cooling of materials with different CTE in a lap joint configuration and (c) superposition of the resultant {(a)+(b)} interfacial residual stresses in the Al plate.

The lower values of residual stress in the Al plate is due to its lower yield strength (~ 50 MPa). However, due to the presence of multiple origins of residual stresses at the dissimilar joint, the quantitative comparison of each contribution becomes challenging. But, the qualitative representations agree well with the theoretical origins of the residual stresses, while the interfacial effect (mismatch in CTE, Fig. 10b and 11b) becomes dominant in both steel and aluminum plates near the interface confirming a clear trend of mirror effect in both materials. That is, the steel structure has a highly heterogeneous microstructure, the bottom of the steel attached to a high thermal conductive aluminum and the aluminum melts during the process so the bottom surface may reach a maximum temperature of about 750°C. Thus, near the interface the phase transformation in the steel plate will not significantly contribute to residual stress changes. Therefore, the main contribution for the mirroring effect near the interface is expected to be dominated by the mismatch in CTE.

5. Conclusions

Residual stresses at an Al/steel joint produced by Friction Melt Bonding were measured using neutron diffraction technique. First, a small step scan was performed to identify non-destructively the interface position using the diffraction intensities obtained for the steel {211} peaks. The identified interface position reasonably agrees with the actual interface position obtained using scanning electron microscopy. The Full Width at Half Maximum (FWHM) of the steel {211} peaks obtained from the large step line scans was then compared at the mid-thickness of the steel plate. The FWHM distribution concurs with the formation of a martensitic microstructure in the processed zone. The steel {211} peaks and the aluminum {311} peaks are used for the residual stress calculation.

The resultant of the residual stresses along the three components in the mid-thickness of steel plate is close to zero, confirming stresses are physically feasible. Longitudinal residual stresses reveal that the upper steel plate has an overall “M” shape distribution while the lower aluminum shows a “W” shape near the interface. This mirror effect is obvious at the vicinity of the interface and is mainly caused by the mismatch in coefficient of thermal expansion. The additional sources of residual stresses in the steel mainly comes from FSW-like stresses, including the effect of a phase transformation in the processed zone, while the residual stresses in aluminum partly result from the melting-solidification effect.

Acknowledgements

The authors acknowledge the financial support of the Interuniversity Attraction Poles Program from the Belgian State through the Belgian Policy agency, contract of IAP7/21 INTEMATE and the international Neutron Source at Institut Laue-Langevin (ILL) for the provision of beamtime at SALSA (Proposal No. 1-02-212). NJM acknowledges the financial support of FRIA, Belgium. AS and TS acknowledges the financial support of the European Research Council for a starting grant under grant agreement 716678, ALUFIX project.

Supplementary material

Supplementary data associated with this article can be found, in the online version, at « Please note, that the corresponding DOI link will be specified here later during the production».

Conflict of Interest

The authors declare no conflict of interest.

References

Agudo, L., Weber, S., Pinto, H., Arenholz, E., Wagner, J., Hackl, H., Bruckner, J., Pyzalla, A., 2008. Study of microstructure and residual stresses in dissimilar Al/steels welds produced by cold metal transfer, Materials Science Forum. Trans Tech Publ, pp. 347-353.

ASTM E8 / E8M - 16a, 2016. Standard Test Methods for Tension Testing of Metallic Materials. ASTM International, West Conshohocken, PA.

Bruno, G., Fanara, C., Hughes, D.J., Ratel, N., 2006. Procedures for interface residual stress determination using neutron diffraction: Mo-coated steel gear wheel. Nuclear Instruments and Methods in Physics Research Section B: Beam Interactions with Materials and Atoms 246, 425-439.

Chobaut, N., 2015. Measurements and modelling of residual stresses during quenching of thick heat treatable aluminium components in relation to their precipitation state, Laboratoire de simulation des matériaux. École polytechnique fédérale de lausanne.

Chobaut, N., Saelzle, P., Michel, G., Carron, D., Drezet, J.-M., 2015. Quench-induced stresses in AA2618 forgings for impellers: a multiphysics and multiscale problem. JOM 67, 984-990.

Crucifix, S., van der Rest, C., Jimenez-Mena, N., Jacques, P., Simar, A., 2015, Modelling thermal cycles and intermetallic growth during friction melt bonding of ULC steel to aluminium alloy 2024-T3, Science and Technology of Welding and Joining 20, 319-324.

Deplus, K., Simar, A., Haver, W.V., Meester, B.d., 2011. Residual stresses in aluminium alloy friction stir welds. The International Journal of Advanced Manufacturing Technology 56, 493-504.

Ezeilo, A., Webster, G., Webster, P., Roth, M., Muster, W., 1991. Comparison of X-ray and neutron diffraction determinations of residual stresses in a laser treated martensitic steel, Proc. of the 2nd European Conf on Adv Materials and Processes (Eds TW Clyne and PJ Withers), Euromat, pp. 389-394.

Gan, W.M., Hofmann, M., Ventzke, V., Randau, C., Huang, Y.D., Kriele, A., Brokmeier, H.G., Mueller, M., 2017. Microstructure and Residual Stress in Rotary Friction Welded Dissimilar Metals of AA7020 Aluminium Alloy with 316L Steel, Materials Science Forum. Trans Tech Publ, pp. 572-577.

Hutchings, M.T., Withers, P.J., Holden, T.M., Lorentzen, T., 2005. Introduction to the characterization of residual stress by neutron diffraction. CRC press, Boca Raton, USA.

ISO/TS 21432:2005, 2010. Non-destructive testing -- Standard test method for determining residual stresses by neutron diffraction. International Organization for Standardization, Geneva, CH.

Jacques, P.J., Furnemont, Q., Godet, S., Pardoen, T., Conlon, K., Delannay, F., 2006. Micromechanical characterisation of TRIP-assisted multiphase steels by in situ neutron diffraction. Philosophical magazine 86, 2371-2392.

Jimenez-Mena, N., Drezet, J.-M., Jacques, P., Pirling, T., Sapanathan, T., Simar, A., 2017. Characterisation of a dissimilar Al-to-steel joint. From process parameters to residual stresses and mechanical properties. Institut Laue-Langevin (ILL), doi:10.5291/ILL-DATA.1-02-212.

Jimenez-Mena, N., Jacques, P.J., Drezet, J.-M., Simar, A., 2018. On the prediction of hot tearing in Al-to-steel welding by friction melt bonding. Metall and Mat Trans A, 1-13.

Joseph, A., Rai, S.K., Jayakumar, T., Murugan, N., 2005. Evaluation of residual stresses in dissimilar weld joints. International Journal of Pressure Vessels and Piping 82, 700-705.

Kim, Y.C., Fuji, A., North, T.H., 1995. Residual stress and plastic strain in AI51 304L stainless steel/titanium friction welds. Materials Science and Technology 11, 383-388.

Kou, S., 2003. Welding metallurgy. John Wiley & Sons, New Jersey, USA.

Kumar, N., Mishra, R.S., Baumann, J.A., 2013. Residual stresses in friction stir welding. Butterworth-Heinemann, Oxford, UK.

LAMP, accessed 10/03/2017. The Large Array Manipulation Program. Institut Laue-Langevin (ILL).

Massalski, T.B., Murray, J.L., Bennrtt, L.H., Hugh, B., 1990, Binary alloy phase diagrams, ASM International, Ohio, USA

Pirling, T., 2011. Precise analysis of near surface neutron strain imaging measurements. Procedia Engineering 10, 2147-2152.

Pirling, T., Bruno, G., Withers, P.J., 2006. SALSA—A new instrument for strain imaging in engineering materials and components. Materials Science and Engineering: A 437, 139-144.

Prime, M.B., Gnäupel-Herold, T., Baumann, J.A., Lederich, R.J., Bowden, D.M., Sebring, R.J., 2006. Residual stress measurements in a thick, dissimilar aluminum alloy friction stir weld. Acta Materialia 54, 4013-4021.

Šaroun, J., Kornmeier, J.R., Hofmann, M., Mikula, P., Vrana, M., 2013. Analytical model for neutron diffraction peak shifts due to the surface effect. Journal of Applied Crystallography 46, 628-638.

Simar, A., Avettand-Fènoël, M.N., 2017. State of the art about dissimilar metal friction stir welding. Science and Technology of Welding and Joining 22, 389-403.

Smith, C.W., 1979. Fracture Mechanics: Proceedings of the Eleventh National Symposium on Fracture Mechanics. ASTM International.

Tanaka, T., Morishige, T., Hirata, T., 2009. Comprehensive analysis of joint strength for dissimilar friction stir welds of mild steel to aluminum alloys. Scripta Materialia 61, 756-759.

van der Rest, C., Jacques, P.J., Simar, A., 2014. On the joining of steel and aluminium by means of a new friction melt bonding process. Scripta Materialia 77, 25-28.

van der Rest, C., Simar, A., Jacques, P.J., 2013. Method for welding at least two layers. Patent No. WO 2013164294 A1.

Wang, X.-L., Spooner, S., Hubbard, C., 1998. Theory of the peak shift anomaly due to partial burial of the sampling volume in neutron diffraction residual stress measurements. Journal of applied crystallography 31, 52-59.

Waterschoot, T., Cooman, B.C.D., Vandeputte, S., Conlon, K., 2003. Neutron diffraction study of the low-temperature ageing of martensite in dual-phase steel. Zeitschrift für Metallkunde 94, 424-435.